Fully Integrated FMCW LiDAR Optical Engine on a Single Silicon Chip

Keyvan Sayyah ⓘ, Raymond Sarkissian, Pamela Patterson, Biqin Huang, Oleg Efimov, Danny Kim, Ken Elliott, Louis Yang ⓘ, and David Hammon

Abstract—We present the demonstration of two novel chip-scale FMCW LiDAR optical engines in which all photonic components, including the laser sources, were integrated on single silicon chips. Using the first LiDAR chip design, with an integrated distributed Bragg reflector laser and grating couplers as input/output ports for the receive/transmit light, we demonstrated a maximum range of 28 m limited by transmit light output power of 2 mW. We further demonstrated a maximum range of 75 m using a second LiDAR chip architecture having an on-chip sampled grating distributed Bragg reflector master laser with integrated power amplifier in which the local oscillator light was obtained from the laser back facet. This maximum range can be further increased by improving the laser linewidth. The measured range dependence of the FMCW signal level for both LiDAR chips agreed well with theory. The chip-scale FMCW LiDAR optical engines can be used in conjunction with a variety of off-chip two dimensional beam scanners to realize a chip-scale scanning LiDAR solution. To the best of our knowledge, this is the first published demonstration of fully integrated FMCW LiDAR optical engines on a single silicon chip.

Index Terms—Chip-scale, distributed Bragg reflector laser, FMCW LiDAR, heterogeneous integration, laser linewidth, local oscillator, optical engine, sampled grating distributed Bragg reflector laser, signal-to-noise ratio.

I. INTRODUCTION

LIGHT detection and ranging (LiDAR) sensor technology has been used extensively in the past decades for a multitude of diverse applications such as 3-dimensional (3D) terrain mapping from airborne platforms [1], lunar landing [2], atmospheric metrology [3], agricultural crop mapping [4], oceanography (depth and composition mapping) [5], forest canopy measurements [6], soil profiling [7], wind speed measurements [8], forensics [9], and oil and gas exploration [10] to name a few. However, in recent years, the key use case for LiDAR has been for autonomous vehicles (AV) and advanced driver assistance systems (ADAS) [11]–[15]. This application, which has gained tremendous momentum in the last few years, needs a new class of LiDAR sensors which are very compact in size

(cigarette box dimensions) and low-cost (<$100), as multiple such devices are needed for a single vehicle. The recent advent of integrated photonic platforms, based on silicon (Si) [16], silicon nitride (SiN) [17] and III-V semiconductors [18], has made the realization of new class of chip-scale LiDAR architectures possible for the automotive use, as well as for other applications.

Of the two main LiDAR modalities - pulsed time-of-flight (ToF) [19] and frequency modulated continuous wave (FMCW) [20] - the latter is better suited for a chip-scale implementation. This is mainly due to the lower peak laser power requirement for FMCW LiDAR, which makes the integration of the semiconductor laser on the LiDAR chip more practical. Furthermore, FMCW LiDAR requires a much lower photoreceiver electrical bandwidth, which results in lower cost electronics. Other advantages of FMCW over ToF LiDAR include simultaneous range and velocity measurements, and interference immunity from solar glare and other nearby LiDAR sensors [21]. The main disadvantage of FMCW LiDAR is its more complex system relative to a ToF sensor. A chip-scale implementation, however, will eliminate this drawback.

There have been a few reported chip-scale FMCW LiDAR demonstrations to date [22]–[27]. Martin *et al.* demonstrated a FMCW LiDAR with up to 60 m range based on a Si photonic platform in which the waveform calibration, scanning system and balanced photodetectors were implemented on-chip in combination with an array of fiber circulators and collimators [22]. Furukado *et al.* used a combination of a Si photonic crystal slow-light Mach-Zehnder modular and a photonic crystal optical antenna array on separate chips in conjunction with a fiber delay line to demonstrate FMCW LiDAR functionality [23]. Isaac *et al.* developed an InP-based photonic integrated circuit (PIC) transceiver chip for FMCW LiDAR which included a sampled grating distributed Bragg reflector (SGDBR) tunable laser generating the transmit light, a frequency discriminator for providing laser frequency stabilization and modulation via feedback control and balanced photodiodes in the receiver section [24]. However, no FMCW LiDAR functionality was demonstrated.

The recent focus on developing chip-scale FMCW LiDAR has been on the optical phased array (OPA) LiDAR architecture. Poulton *et al.* demonstrated 3D FMCW OPA LiDAR with target detection range of up to ∼10 m using separate transmit and receive 512-element OPAs (∼10 mm^2 aperture size) with Si PN junction based phase shifters using an off-chip high power (200 mW) laser source fiber coupled to the OPA chip [25]. They achieved 2D LiDAR beam steering by optical phase control

(via the integrated phase shifters) and wavelength scanning in the directions perpendicular and parallel to the array elements, respectively. The same group demonstrated 2D FMCW LiDAR with up to ~180 m detection range using a variant of the OPA described above with a bigger aperture size in which only 1D wavelength scanning was employed. The bigger aperture size and absence of phase shifters in the arrays (which reduced the overall optical loss) enabled a longer range detection capability [25]. Miller *et al.* also demonstrated 512-element Si-based optical phased arrays with integrated low-loss thermal phase shifters for FMCW LiDAR applications [26]. They reported that this OPA with an aperture size of ~0.7 mm^2 is adequate for 10 m ranging using an external laser with an optical power of 50 mW fiber coupled to the OPA chip. There has been yet another demonstration of chip-scale FMCW OPA LiDAR in which 128-element transmit and receive optical phased arrays with a small aperture size of ~0.13 mm^2 were used in conjunction with an external laser fiber coupled to the OPA chip [27]. The novel feature of this demonstration was the 3D heterogeneous integration of the OPA chip with the CMOS chip containing the transimpedance amplifier (TIA) and the analog-to-digital converter (ADC) circuits in the photoreceiver. Using this OPA LiDAR chip, they demonstrated target detection ranges of up to 30 cm with 3 cm range resolution.

In all chip-scale FMCW LiDAR demonstrations published to date, the laser source has been external to the chip and coupled to it via an optical fiber. In this paper, we demonstrate two implementations of an integrated photonic-based FMCW Li-DAR optical engine in which the *laser source is heterogeneously integrated on the same Si chip containing the transmitter and receiver sections of the LiDAR engine*, enabling range detection of up to 75 m. To the best of our knowledge, this is the *first published demonstration* of such a chip-scale FMCW LiDAR.

The organization of this paper is as follows. In Section II, we will first describe some of the FMCW LiDAR fundamentals including theoretical signal and noise models, which will be compared to the measured results of our chip-scale LiDAR optical engines. This is followed in Section III with a description of two chip-scale FMCW LiDAR optical engine architectures that we will subsequently demonstrate. In Section IV, we will present some of the fabrication details for the realization of these LiDAR chips, followed by a description of the experimental results of their range and range resolution measurements in Section V. Finally, we give a summary of this work together with some concluding remarks in Section VI

II. FMCW LiDAR Fundamentals

In this Section, we will first describe some of the fundamentals of FMCW LiDAR operation including the dependence of target range, range resolution and velocity measurements on various system parameters. Fig. 1 shows the conventional optical frequency ramp (chirped) signal of the laser transmitter of a FMCW LiDAR sensor (blue waveform) together with the time-delayed Δt receive signal for a moving target (red waveform), and the extent of the transmitter optical frequency modulation defined as Δf.
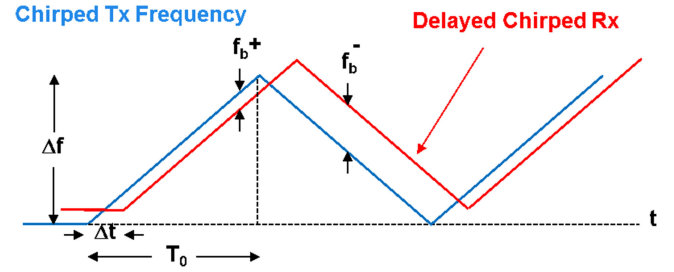

Fig. 1. Schematic of a typical FMCW LiDAR laser modulation ramp (blue) and time-delayed receive signal (red) waveforms, assuming that the target is moving towards the LiDAR transceiver.

One of the key advantages of FMCW LiDAR over pulsed ToF LiDAR is its ability for simultaneous detection of the range and velocity of a moving target. Assuming the target is moving toward the LiDAR sensor with radial velocity (v), the instantaneous target range (R) and velocity are given by [28], [29]:

$$R = \frac{cT_0 \left(f_b{}^- + f_b{}^+ \right)}{4\Delta f} \tag{1}$$

$$v = \frac{c \left(f_b{}^- - f_b{}^+ \right)}{4} \tag{2}$$

Where T_0 is the up and down ramp times, $f_b{}^+$ and $f_b{}^-$ are the generated FMCW beat signal frequencies (difference between transmit and the time-delayed receive optical frequency) in up and down ramps, respectively, and c is the speed of light. The above relationship assumes the FMCW LiDAR transmitter is generating a perfectly linear optical frequency ramp signal.

The range resolution (ΔR) and range accuracy (δR) of FMCW LiDAR are given by the following relationships:

$$\Delta R = \frac{cT_0}{2\Delta f T_{int}} \tag{3}$$

$$\delta R = \frac{\Delta R}{\sqrt{SNR}} \tag{4}$$

Where T_{int} is the integration time for LiDAR signal detection whose maximum value is defined by T_0-Δt, and SNR is the LiDAR signal-to-noise ratio. In practical cases where the optical frequency ramp is linear only during a portion of the ramp time, defined by T_{int}, the range resolution is degraded from its transform limited maximum value of $c/2\Delta f$ by a factor of T_0/T_{int} as indicated in Eq. (3).

The FMCW LiDAR SNR is the ratio of the received beat signal and the system noise level. The received FMCW beat signal is derived as follow. The optical power impingent on a target is given by:

$$P_{target} = \frac{P_{Tx}}{A_{beam}} A_{target} T_{atm} \tag{5}$$

Where, A_{beam} and A_{target} are the transmit beam cross-sectional area at the target and the target area, respectively, P_{Tx} is the LiDAR transmit optical power, and T_{atm} is the one-way atmospheric transmission factor. In Eq. (5), it is assumed that the transmit beam cross-sectional area is larger than the target

area. The received optical power is obtained by integrating the reflected radiance over the illuminated area at the target within the receiver field-of-view. For a pure Lambertian target, the received optical power, P_{Rx}, can be written as [30]:

$$P_{Rx} = P_{target}\frac{\rho_T}{\pi}T_{atm}\int_0^{2\pi}d\varphi\int_0^{\theta_{Rx}}sin\theta cos\theta d\theta$$

$$= A_{target}\;\int_0^{2\pi}d\varphi\int_0^{\theta_{Rx}}sin\theta L_0 cos\theta d\theta \tag{6}$$

Where,

$$L_0 = \frac{\rho_T}{\pi}\;\frac{P_{Tx}}{A_{beam}}T_{atm}^2 \tag{7}$$

Here, ρ_T is Lambertian target reflectance and θ_{Rx} is the LiDAR receiver field-of-view (FOV) given by $\theta_{Rx} = \frac{D_{Rx}}{2R}$, where D_{Rx} is the receive aperture and R is the range to target. Combining Eqs. (5), (6) and (7) results in the following relationship for the received LiDAR receive optical power:

$$P_{Rx} = P_{Tx}\;\rho_T T_{atm}^2\frac{A_{target}}{A_{beam}}\;\frac{d_{Rx}^2}{4R^2}$$

$$= P_{Tx}\;\rho_T T_{atm}^2\frac{A_{target}}{A_{beam}}\frac{A_{Rx}}{\pi R^2} \tag{8}$$

In the more relevant case in which the transmit *beam cross-sectional area is less than the target area* ($A_{beam} < A_{target}$) for narrowly divergent LiDAR transmit beams, Eq. (8) above for the receive optical power reduces to:

$$P_{Rx} = P_{Tx}\rho_T T_{atm}^2\frac{A_{Rx}}{\pi R^2} = P_{Tx}\;\rho_T T_{atm}^2\frac{d_{Rx}^2}{4R^2} \tag{9}$$

Substituting for $T_{atm}^2 = e^{-2\alpha_{atm}R}$, where α_{atm} is the atmospheric extinction coefficient, and considering that a fraction of the photons at the receive aperture reach the receiver port for optical mixing with the local oscillator due to the overall receiver collection and transport efficiency, η_{Rx}, as well as depolarization at the target and during atmospheric transmission, η_{pol}, the following relationship for the LiDAR receive optical power at the receiver optical mixing port, P_{Rx0}, is obtained:

$$P_{Rx0} = P_{Tx}\;\rho_T\frac{d_{Rx}^2}{4R^2}\eta_{Rx}\eta_{pol}e^{-2\alpha_{atm}R} \tag{10}$$

After optical mixing and detection by dual balanced photodetectors, the peak beat current of the received FMCW LiDAR signal, I_S, is given by the following relationship [29] :

$$I_S^2 = 2\eta_{PD}^2 P_{Rx0}P_{LO}e^{\frac{-4\pi\Delta\nu R}{c}} \tag{11}$$

Where, η_{PD} is the photodetector responsivity, P_{LO} is the local oscillator (LO) optical power at the mixing port, and $\Delta\nu$ is the effective linewidth of the laser source. The transimpedance amplifier (TIA) connected to the common node of the dual photodetectors converts this photocurrent to an equivalent peak beat signal voltage determined by its transimpedance gain, R_F.

The FMCW LiDAR system noise level is composed of four main contributions: (1) photodetector shot noise, (2) photoreceiver thermal noise, (3) TIA noise and (4) analog-to-digital converter (ADC) quantization noise. The overall FMCW system noise current, I_N, is given by [29]:

$$I_N^2 = 2q\eta_{PD}P_{LO}B_e + \frac{4KTB_e}{R_F} + NEP^2\eta_{PD}^2B_e$$

$$+ \left(\frac{V_{ADC}}{R_F}\right)^2\frac{1}{12(2^N - 1)^2 f_{ADC}}B_e \tag{12}$$

Where, B_e is the signal processing electrical bandwidth (inverse of the LiDAR signal integration time, t_{int}), K is the Boltzmann constant, T is the sensor operating temperature, NEP is the noise equivalent power of the TIA, V_{ADC} is the ADC input voltage range, N is the ADC effective number of bits (ENOB) and f_{ADC} is the ADC bandwidth The 4 terms on the right hand side of Eq. (12), from left to right, correspond to the shot noise, thermal noise, TIA noise and ADC quantization noise, respectively. Using (11) and (12) the FMCW LiDAR $SNR = \frac{I_s^2}{I_N^2}$ then becomes as shown in (13) at the bottom of this page.

The FMCW LiDAR beat signal strength, and hence the SNR, is strongly dependent on the effective linewidth of the laser source for target ranges larger than the laser coherence length. The effective linewidth of the laser can be theoretically derived from the integration of its frequency noise power spectral density in the offset frequency range from the inverse of the maximum LiDAR time delay (range) to the onset of the Lorentzian noise. We will apply the signal and noise model described above to the two chip-scale FMCW LiDAR implementations described in this paper and compare them to the measurement results in Section V.

The scanning FMCW LiDAR point cloud rate is partially dependent on the frequency tuning speed (*1/2T$_0$* in the waveform shown in Fig. 1), among other parameters. The frequency tuning speed is limited by two major factors, namely, the system level requirements such as the maximum distance to target, frame rate, range resolution etc., and the intrinsic limitations imposed by the laser itself. For example, for ranging up to 150 m the delay time will be $\sim$1 μs. This means that the optical frequency ramp time has to be >1 μs. With 10 μs triangular waveform ramp time, the modulation speed will be 50 kHz. For the lasers used in this study, frequency excursions in the range of 1-2 GHz could be achieved without introducing un-recoverable non-linearity correction. Consequently, the highest frequency tuning speeds for the lasers used in this work were between 100-200 MHz/μs. The intrinsic laser factor is a trade-off between the modulation speed and the extent of frequency modulation (excursion), which is dependent on the laser design used.

$$SNR = \frac{2\eta_{PD}^2 P_{Rx0}P_{LO}e^{\frac{-4\pi\Delta\nu R}{c}}}{2q\eta_{PD}P_{LO}B_e + \frac{4KTB_e}{R_F} + NEP^2\eta_{PD}^2B_e + \left(\frac{V_{ADC}}{R_F}\right)^2\frac{1}{12(2^N-1)^2 f_{ADC}}B_e} \tag{13}$$
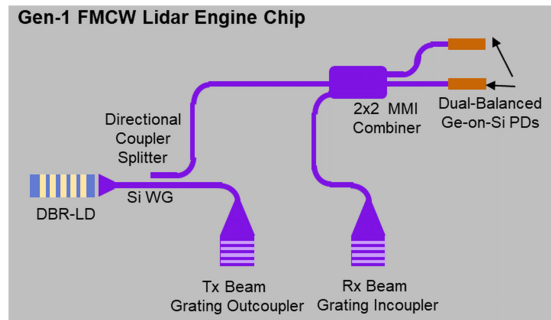
Fig. 2. Schematic of the first generation (Gen-1) FMCW LiDAR engine chip with a heterogeneously integrated DBR laser diode.

Fig. 3. Schematic of the second-generation (Gen-2) FMCW LiDAR engine chip with a heterogeneously integrated InP MOPA laser source.

III. Chip-Scale FMCW LiDAR Optical Engine Architectures

In this work, we developed two novel chip-scale FMCW LiDAR optical engine architectures in which the laser source was heterogeneously integrated on the LiDAR Photonic Integrated Circuit (PIC) chip. Fig. 2 shows the optical schematic of our first generation (Gen-1) LiDAR Si photonic chip which consists of a heterogeneously integrated InP based distributed Bragg reflector (DBR) laser, two grating couplers, a 1×2 directional coupler (DC) splitter, a 2×2 multi-mode interference (MMI) coupler, and dual-balanced Ge-on-Si photodiodes. Light generated by the integrated DBR laser diode and coupled to the Si waveguide network is split by the 1:2 DC splitter in a 90:10 ratio; with the major portion outcoupled from the chip via a grating coupler as the LiDAR transmit light. The remainder of the laser light is used as an on-chip local oscillator (LO) which is optically mixed with the FMCW LiDAR coherent receive light using the 2×2 MMI coupler. The receive light is coupled to the chip via a second grating coupler. The output waveguides of the MMI coupler feed dual-balanced Ge-on-Si photodiodes resulting in the elimination of the laser relative intensity noise (RIN). For LiDAR range measurements described in this paper, transmit and receive lights outcoupled from and incoupled to the chip are collimated and focused using off-chip lenses, respectively, and subsequently combined into a single transmit/receive aperture via a free-space optical circulator. For scanning FMCW LiDAR, the off-chip transmit and receive light beams can be steered in both azimuthal and elevational directions using 2D MEMS or other 2D beam scanners. In this work, we only demonstrated the functionality of this chip as a FMCW range finder, as described in Section V.

The schematic of our second-generation (Gen-2) FMCW LiDAR optical engine chip is shown in Fig. 3. This LiDAR chip also has a heterogeneously integrated laser source consisting of an InP-based master oscillator power amplifier (MOPA) architecture.

The LiDAR transmit light is emitted directly into free-space from the power amplifier side of the MOPA structure and not propagated on-chip in order to maximize the optical power on target. In this novel chip architecture, the local oscillator light is d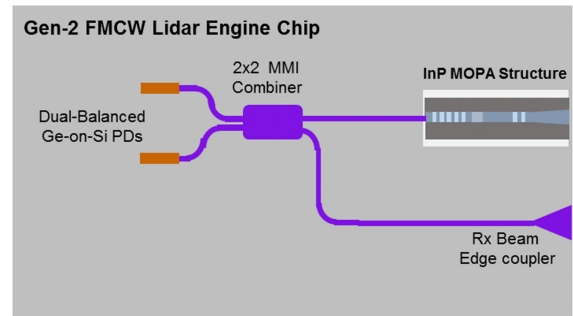irectly obtained from the back facet of the master laser of the MOPA structure, which is coupled to the Si waveguide via a specially designed angled edge coupler.

The LiDAR receive light is coupled to the chip via an edge coupler using a free-space lens, and is subsequently optically mixed with the on-chip LO light via a 2×2 MMI coupler. The output of this coupler feeds a dual-balanced Ge-on-Si photodiodes pair, similar to the Gen-1 chip architecture. Again, a 2D beam scanner such as MEMS, or other mechanical or non-mechanical scanners, can be used after the circulator to obtain 3D LiDAR images. In this study, we demonstrated LiDAR range measurements using this chip without beam scanning, as described in Section V below.

IV. LiDAR Chip Fabrication

A. First Generation (Gen-1) Chip-Scale FMCW LiDAR

One of the key features of this LiDAR chip is the heterogeneous integration of a DBR laser diode with high coupling efficiency to the Si waveguide network on the chip. To accomplish this, we successfully developed a laser facet etch, custom edge couplers, and aligned bonding processes for the laser die integration to the LiDAR Si photonic chip. Our laser integration process is passive, based on lithographically defined alignment marks on the laser and the PIC. Facet etching of the laser is critical since the dimensional control of cleaving is at least an order of magnitude larger than lithographic control and the gap between the butt coupled laser and waveguide is critical to achieving efficient coupling.

We worked closely with a laser diode company to develop DBR laser diode chips designed for our heterogeneous integration scheme. Features such as bond alignment targets to the laser ridge ensured the best possible overlay accuracy to the laser facet for integration. Since the facet etch was developed and performed at HRL, close coupling of custom process flows was required between HRL and the laser company. For the Gen-1 process, our laser facet etch was done at wafer level prior to backside metal formation, AR coating, and cleaving processes done at the laser company. The facet etch process produced smooth facets (Fig. 4a) and the average output power for DBR lasers processed in the same lot were measured at 69 mW and 65 mW for cleaved and etched facets, respectively. This small power difference indicates a good dry etch process resulting in an optically smooth laser diode output facet.

(a) Laser array die with etched facets

(b) PIC with edge couplers, etched recess, and Au bond metal

(c) Laser die aligned and bonded to PIC with Au-Au thermo-compression
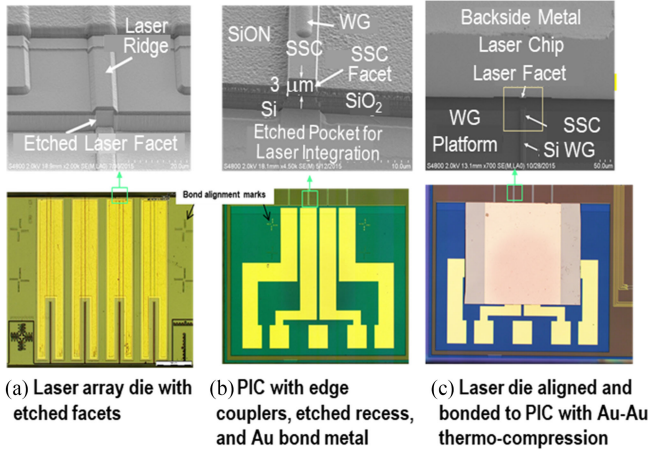
Fig. 4. Images showing Gen-1 component fabrication and integration (a) laser facet etch (b) edge coupler added to PIC wafer and (c) on chip integration of butt- coupled laser die and waveguide edge couplers on PIC die.

(a) MOPA with back etched facet

(b) PIC with etched edge coupler and recess for laser

(c) Laser die aligned and bonded to PIC with Au-Au thermo-compression

Fig. 5. Images showing Gen-2 component fabrication and integration (a) laser facet etch, (c) edge coupler added to PIC wafer, and (c) on PIC integration of butt coupled back facet MOPA die.

(a)   (b)

Fig. 6. (a) Photograph of a Gen-1 FMCW LiDAR engine chip showing the positions of the DBR laser bond pads, edge couplers (EC) and grating couplers (GC) before heterogeneous integration of the laser. (b) Measured LI characteristics of a DBR laser diode with etched facet before and after heterogeneous integration on the LiDAR chip demonstrating a high coupling efficiency of 88%.

The Si photonic components for both generations of our FMCW LiDAR chips were fabricated using imec's Si photonics foundry process [31]. Fabrication processes for the edge couplers designed to maximize the coupling between the laser and waveguides were developed at HRL. We performed the post processing required to add SiON based edge couplers to the imec-fabricated PIC. This required receipt of the wafers prior to final metallization of the photodiodes; metallization was performed at HRL with no degradation to the photodiode performance. We also developed the processes needed to add a recessed pocket to the PIC to achieve vertical alignment of the laser and edge coupler (Fig. 4b). The depth of the recess etch in conjunction with a subsequent gold deposition was used to tune the laser die height to within 0.5 microns of the designed value with respect to the edge coupler. The laser to PIC die-to-die integration was performed on an SET-FC300 die bonder with submicron accuracy. The DBR laser die were aligned to the PIC and an Au-Au thermo-compression bond was formed between the Au coated laser ridge and Au traces on the PIC wafer (Fig. 4c). The bond formed the electrical contact to the laser ridge while a wire bond was used to contact the backside (not shown).

B. Second Generation (Gen-2) Chip-Scale FMCW LiDAR

Our Gen-2 fabrication processes built on those developed for Gen-1 integrated lasers on PIC, but significant additional development was required for a new MOPA laser design from a second laser vendor. For the Gen-2 design, rather than the front facet coupling to the PIC waveguide as in Gen-1, the back facet of the MOPA was butt-coupled to the waveguide.

As in the Gen-1 LiDAR chip, the alignment between the laser and PIC was passive, hence, laser facet etching was required (Fig. 5a). The MOPA laser required a deeper etch on the PIC to align the laser and edge coupler facets in the vertical direction (Fig. 5b). This need arose from a lower position of the laser mode relative to the epi layer and thicker metal on the laser using with the same processes described for the Gen-1 integration.
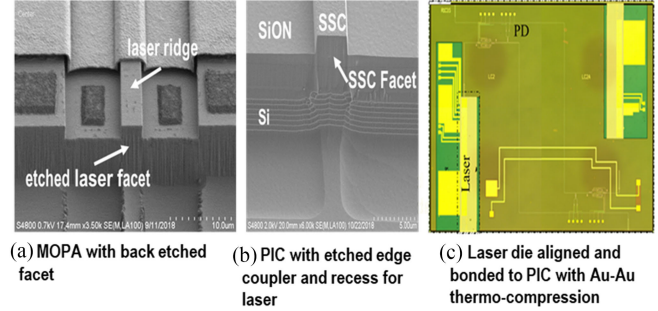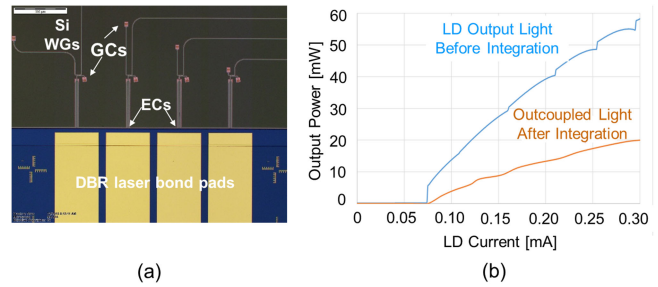
However, the MOPA structure had multiple contacts fanned out to the PIC through the Au-Au bond, as can be seen in Fig. 5c.

In both Gen-1 and Gen-2 on-chip laser integrations, we demonstrated coupling efficiencies within 10 to 20 percent of expected values for the best devices. It should be mentioned that we also observed some chip-to-chip variations in the coupling efficiency. The source of this variation is not completely understood and occurred even when measured misalignment (lateral and gap) between the laser and edge coupler facets was controlled to within $\pm 0.5\mu m$ of designed values.

The optical coupling between the laser facets and the Si chip were achieved using custom designed edge couplers (spot size converters), as described above. The modal dimensions of the laser light near the edge of the silicon chip is in a few microns-range for realistic coupling distances. On the other hand, the mode in the silicon waveguide is tightly confined to the core of the Si waveguide with dimensions of ∼450 nm x 220 nm. This modal mismatch introduces a significant loss mechanism that is addressed by the integrated photonic spot-size converters (SSCs) that we properly designed and implemented in both Gen-1 and Gen-2 chip-scale lidar architectures.

V. EXPERIMENTAL RESULTS

A. First Generation (Gen-1) Chip-Scale FMCW LiDAR

Fig. 6(a) shows a photograph of a Gen-1 LiDAR chip indicating the positions of 4 bond pads where a laser die with 4 identical
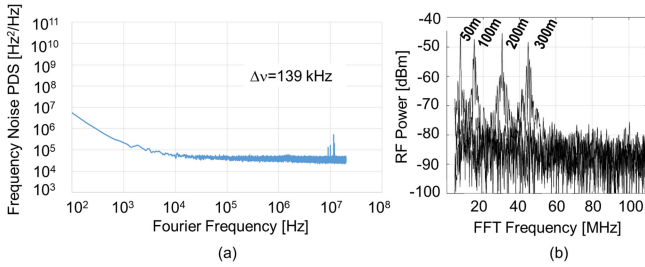
Fig. 7. (a) Measured frequency noise spectrum of a DBR laser diode integrated on a Gen-1 LiDAR chip indicating a Lorentzian linewidth of ∼90 kHz and an effective linewidth of ∼140 kHz. (b) Measured beat signal spectrum of a FMCW LiDAR using the Gen-1 chip and fiber delays lengths of 50-300 m.
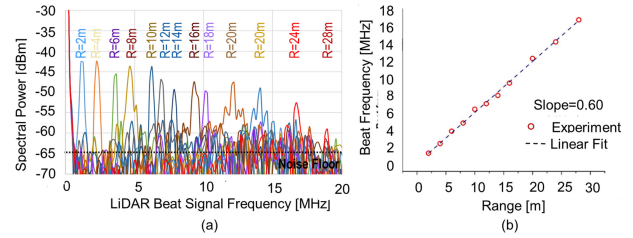

Fig. 8. (a) Measured FMCW beat signal FFT spectra for the Gen-1 chip-scale LiDAR optical engine as a function of discrete target ranges from 2-28 m. The FFT bin size is 167 kHz resulting from an integration time of 6 μs. (b) Plot of the measured FMCW beat signal FFT vs. range showing a linear dependence with a slope of 0.6 MHz/m.

DBR lasers is heterogeneously integrated with precise alignment relative to custom designed edge couplers. One of these lasers is coupled to the Gen-1 FMCW LiDAR photonic circuitry (shown in Fig. 2), while the other 3 are coupled to different photonic test circuits on the chip. One of these test circuits is used to measure the coupling efficiency of the DBR laser diode to the standard Si-on-insulator (SOI) waveguide (450×220 nm^2 cross-section) on the chip.

Fig. 6(b) shows the measured light-current (LI) characteristics of one of these DBR lasers before (blue curve) and after (orange curve) integration via a photonic circuit consisting of the laser, a 90:10 directional coupler, a 3 mm long Si waveguide, and an output grating coupler. We extracted a laser-to-Si waveguide coupling efficiency of ∼88% using measured Si waveguide propagation loss of 2 dB/cm and grating coupler efficiency of 3 dB.

As mentioned in Section II above, the effective linewidth of the laser source is one of the key parameters in FMCW LiDAR systems, as it determines its coherence length and hence affects the LiDAR SNR and maximum range (see Eqs. 11 and 13). To this end, we first used the Gen-1 LiDAR chip in conjunction with an optical fiber delay line to measure the FMCW beat signal as a function of the delay length in order to measure the laser coherence length. Fig. 5(a) shows the measured frequency noise spectrum of one of the integrated DBR lasers demonstrating a Lorentzian linewidth of ∼90 kHz (∼30 Hz^2/Hz x π) and an effective integrated linewidth of ∼140 kHz (as measured using a delayed self-heterodyne technique). The measured beat signal of this LiDAR chip as a function of the fiber delay length varying between 50-300 m is shown in Fig. 7(b). For this measurement, the LiDAR transmit light is coupled to the delay fiber via the on-chip transmit grating coupler and the output of the fiber is coupled back to the chip using the receive grating coupler. The measured data indicate a sharp FMCW beat signal with even using a fiber delay length of 300m, which corresponds to a free-space LiDAR range of 225m, consistent with the measured narrow effective linewidth of the integrated DBR laser diode.

For the Gen-1 LiDAR chip measurements reported here, we developed a laser optical frequency linearization method that relies on optimizing the injection current waveform by probing the beat-frequency-versus-range curve for linearity in an iterative fashion. A functional form was empirically developed that best linearized the optical frequency ramp by adjusting the

weighted coefficients in this waveform. We were able to linearize the frequency modulation response of the integrated DBR laser diode through the iterative procedure noted above.

This optical frequency linearization method can be best understood by considering Fig. 1. If the frequency chirping is linear in time, an increase in the LiDAR range results in a linearly proportional change in the beat frequency. We used this very fact to measure the nonlinearity in frequency modulation. That is, we measured the beat-frequency versus range nonlinearity and forced it to become linear by changing the functional coefficients noted above in an iterative fashion.

The Gen-1 FMCW LiDAR chip was then used in conjunction with two free-space lenses, one for collimating the transmit beam outcoupled from the chip and the other to focus the receive beam onto the chip, and a free-space optical circulator, to demonstrate free-space LiDAR range measurements. The chip was mounted on a printed circuit board (PCB) which contained the post photodetection transimpedance amplifier circuitry for the conversion of the FMCW LiDAR beat photocurrent to a proportional analog voltage signal, which was subsequently digitized, and fast Fourier transformed using a digital oscilloscope. Fig. 8(a) shows the measured FMCW beat signal FFT spectra for a Gen-1 LiDAR chip with 2.4 mW transmit beam optical power and on-chip LO optical power of 300 μW at different ranges using a Lambertian target. The LiDAR transmit and receive apertures were both 9 mm. We measured a maximum range of 28 m with the system noise floor at ∼−65 dBm, as shown in Fig. 8(a).

Fig. 8(b) shows the linear dependence of the measured FMCW beat signal frequency on target range for this chip-scale LiDAR optical engine. This indicates proper linearization of the laser optical frequency ramp using the predistortion compensation algorithm described above. The measured slope of the FMCW receive signal beat frequency vs. range is ∼0.6 MHz/m for the optical frequency ramp duration of 10 μs used here. Using the theoretical relationship between beat frequency and range for FMCW LiDAR: $\frac{f_b}{R} = \frac{2\Delta f}{cT_0}$ [29], where f_b is the beat signal frequency, R is the LiDAR range, c is the speed of light, Δf is the extent of the optical frequency modulation of the transmit beam and T_0 is the optical frequency ramp duration (see Fig. 1), we extract $\Delta f = 0.9$ GHz. The transform limited LiDAR range resolution is 16.7 cm (Eq. 3), assuming that the entire ramp period is used for FFT integration. In this measurement, however,
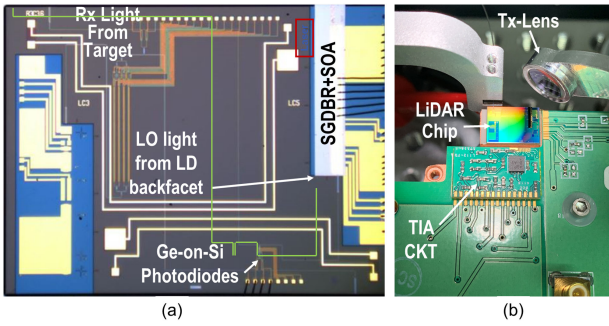
Fig. 9. (a) Photograph of a fabricated Gen-2 FMCW LiDAR optical engine Si photonic chip showing the locations of the heterogeneously integrated SGDBR MOPA laser, the receive and LO light edge couplers, and the dual-balanced Ge-on-Si photodiodes. (b) Photograph of the Gen-2 LiDAR chip mounted on an electronic PCB containing the laser driver and photoreceiver circuitry. Also shown, is the collimating lens for the LiDAR transmit light.
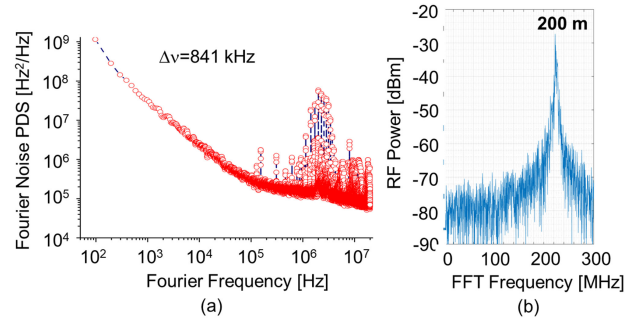

Fig. 10. (a) Measured frequency noise spectrum of the SGDBR MOPA laser integrated on the Gen-2 LiDAR chip indicating a Lorentzian and effective linewidths of 500 kHz and 840 kHz, respectively. (b) Measured FFT beat signal of the Gen-2 FMCW LiDAR chip using a 200 m optical fiber delay line.

we used 60% of the ramp period for FMCW signal integration time (6 μs), resulting in an effective range resolution of $\sim$28 cm.

B. Second Generation (Gen-2) Chip-Scale FMCW LiDAR

The Gen-2 chip-scale FMCW LiDAR optical engine architecture shown schematically in Fig. 3 has 2 major differences relative to the first generation sensor. First, the LiDAR transmit light, generated by a heterogeneously integrated sampled grating distributed Bragg reflector (SGDBR) laser and boosted by an on-chip semiconductor optical amplifier (SOA), is directly free-space coupled and not propagated on the Si chip in order to maximize the transmit optical power, and hence the LiDAR range. Second, the on-chip LO light is obtained from the back facet of the SGDBR laser, amplified using an integrated backside SOA, and coupled to a Si waveguide on the LiDAR chip via a specially designed angled edge coupler with a simulated efficiency of $\sim$88%. This novel on-chip local oscillator light generation architecture resulted in measured LO optical power levels of $>$5 mW.

Fig. 9(a) shows a photograph of a Gen-2 LiDAR Si photonic chip with the integrated SGDBR master oscillator power amplifier (MOPA) laser source. Also shown are the locations of the edge couplers that couple the LiDAR receive light to the receive Si waveguide, and the laser back facet light to the LO Si waveguide, as well as the dual balanced Ge-on-Si photodiodes.

Similar to the Gen-1 chip, the Gen-2 LiDAR Si photonic chip was fabricated using imec's Si photonic foundry process, but the laser integration was performed in-house, as described in Section IV above. For evaluation purposes, the chip was mounted on an electronic printed circuit board (PCB) which contained the laser current driver and photoreceiver circuitry, as shown in Fig. 9(b). Also shown in this figure is the collimating lens for the LiDAR transmit light.

Fig. 10(a) shows the measured frequency noise spectrum of the SGDBR MOPA laser integrated on the Gen-2 LiDAR chip. The Lorentzian linewidth is $\sim$500 kHz and the effective linewidth, as measured using the delayed self-heterodyne method, is $\sim$840 kHz. The effective linewidth, of this laser is a factor of 6 larger than that of the structurally simpler DBR laser

used in the Gen-1 LiDAR chip described above. This is mainly due to the shorter cavity length of the SGDBR laser used here, as well as the addition of some noise resulting from the integrated booster SOA. The main reason for using this laser structure in the Gen-2 LiDAR chip was its higher output power capability of $>$100 mW for the transmit light, as well as the capability of boosting the LO light optical power to increase the FMCW LiDAR range.

For the Gen-2 LiDAR chip measurements, we implemented a different iterative algorithm for obtaining the optimum pre-distorted laser drive current waveform. Here, we adapted a laser optical frequency linearization method from [32] that pre-distorts the injection current ramp to result in a linear laser frequency ramp. The procedure begins with driving the laser with a triangular waveform (ramp n), and subsequently obtaining its corresponding LiDAR beat signal FFT spectrogram vs. time. The instantaneous frequency difference of the desired beat frequency vs. the spectrogram frequency at each point in the ramp is used to weigh the correction for the successive ramp n+1. The convergence of this algorithm usually took 1-3 iterations after which we obtained a narrow FFT beat FWHM mainly limited by the frequency noise of the laser [32], [33]. For some laser diodes, a weighted exponential is sufficient to correct for the nonlinear frequency ramp.

Fig. 11 shows a simulation of the effect of FMCW ramp waveform predistortion compensation on the sharpness and intensity of the beat signal in a LiDAR setup with fiber delay. With a triangular ramp waveform, the resulting FMCW beat signal FFT occupies multiple bins as shown in Fig. 11(a), whereas with proper predistortion compensation the FFT signal is within 1-2 spectral bins as illustrated in Fig. 11(b). Also shown is the spectrogram of the FMCW beat signal that is used in the iterative algorithm for waveform calibration. For a properly compensated ramp waveform, the spectrogram is flat as shown in Fig. 11(b). Overall, for real FMCW LiDAR range measurements, the sharpness of the peak beat signal spectrum is dependent on both the degree of linearity of the optical frequency ramp waveform and the linewidth of the laser source. For a target range approaching the coherence length of the laser, the linewidth factor will dominate the LiDAR SNR.
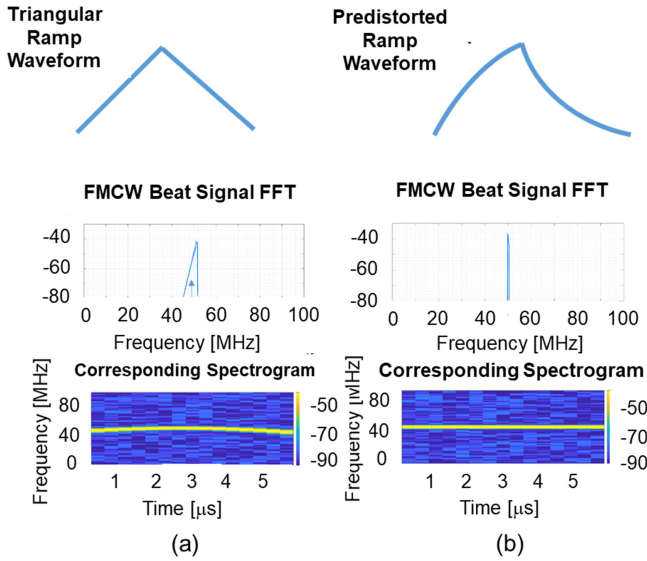
Fig. 11. Demonstration of the effect of laser diode drive current predistortion compensation on the sharpness of FMCW LiDAR beat signal spectrum (b) relative to a triangular ramp waveform (a).
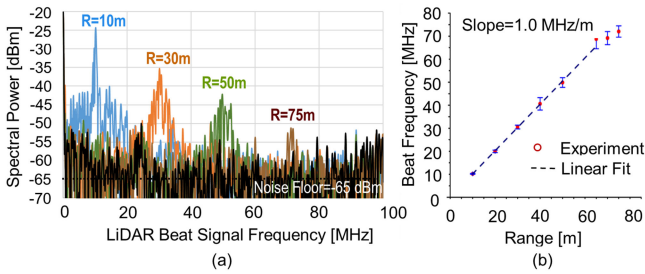

Fig. 12. (a) Measured free-space FMCW beat signal for the Gen-2 LiDAR chip for different Lambertian target ranges from 10-75 m. (b) Linear dependence of the FMCW beat signal frequency on target range indicating a slope of ~1 MHz/m.

Prior to free-space LiDAR range measurements, we evaluated the performance of the Gen-2 LiDAR chip in a setup with an optical fiber delay line. Fig. 10(b) shows the measured FFT spectrum of the FMCW beat signal for this LiDAR configuration using a 200 m fiber delay. This FFT beat signal is not as sharp as the one for the Gen-1 LiDAR chip with the same 200 m fiber delay shown in Fig. 5(b), considering its 3x wider frequency scale. This is consistent with the degraded frequency noise and linewidth of the SGDBR laser used in the Gen-2 LiDAR chip relative to the DBR laser integrated in the Gen-1 chip.

The free-space range measurement data using the Gen-2 chip-scale FMCW LiDAR is shown in Fig. 12(a). A maximum range of 75 m target was detected with a Lambertian target using a LiDAR configuration which included a free-space lens for collimating the transmit light directly emitted by the SGDBR MOPA laser front facet (see Fig. 9(b)) and another lens to focus the receive light onto the input edge coupler of the chip. Fig. 10(b) shows the linear dependence of the FMCW beat signal on the target range indicating good linearization of the laser optical frequency ramp. The measured slope of 1 MHz/m for the data shown in Fig. 10(b) indicate an optical frequency modulation extent of $\Delta f = 1.5$ GHz, resulting in a transform
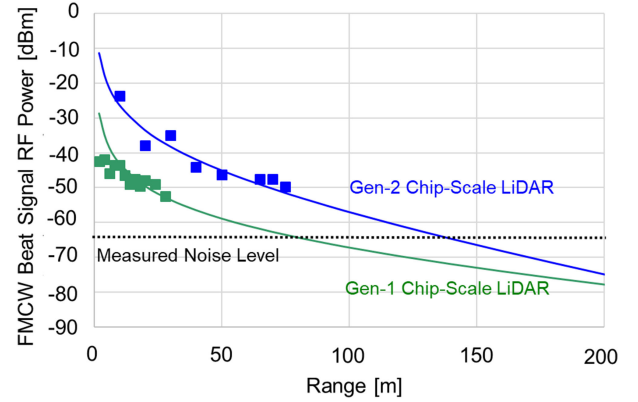

Fig. 13. Comparison of the measured and simulated (using Eq. 11 in the text) FMCW receive beat signal vs. range for the Gen-1 and Gen-2 chip-scale LiDAR. Good agreement is observed using the realistic model parameters listed. Also shown, are the measured and simulated system noise levels.

TABLE I
LIST OF PARAMETERS USED IN EQS. (10) AND (11) TO SIMULATE THE RECEIVED BEAT SIGNAL POWER FOR GEN-1 AND GEN-2 CHIP-SCALE LIDAR SENSORS DEMONSTRATED HERE

	P_{Tx} [mW]	P_{LO} [mW]	$\Delta\nu$ [kHz]	η_{Rx}	d_{Rx} [mm]	B_e [kHz]
Gen-1	2.3	0.3	250	0.35	9	167
Gen-2	80	1.5	650	0.55	9	167
	η_{PD} [A/W]	ρ_T	η_{POL}	R_F [kΩ]	NEP [pW/Hz]	α_{atm} [km^{-1}]
Gen-1	1	0.99	0.6	10	4	0.05
Gen-2	1	0.99	0.6	4.5	4	0.05

limited LiDAR range resolution of 10 cm (see Section V.A above). The effective range resolution, however, was 16.7 cm since we used 60% of the ramp time for beat signal integration.

VI. ANALYSIS AND DISCUSSIONS

In this section, we will use the measured FMCW LiDAR signal and noise data for the two generations of HRL's chip-scale LiDAR optical engine to check the validity of the signal and noise models described in Section II above. Fig. 13 below shows the measured LiDAR beat signal data (in terms of FFT signal electrical peak power level in dBm measured via a digital oscilloscope) vs. range for the Gen-1 and Gen-2 chip-scale LiDAR engines, together with the modeled beat signal according to Eq. (11) converted to an equivalent electrical power using $P_S = \frac{I_S^2 R_F^2}{2R_{in}}$, where R_{in} is the scope input impedance.

The parameters used in the modeled LiDAR signal levels were either accurately measured, taken from the literature, or based on simulations. Table I shows the parameters used in Eqs. (10) and (11) to simulate the Gen-1 and Gen-2 LiDAR receive beat signal levels versus range using a Lambertian target, as illustrated in Fig. 13. The LiDAR parameters listed in this table were defined in Section II. The laser effective linewidth was obtained from a fit of Eq. (11) to the measured data, resulting in a good match with the independently measured linewidth described above for the two lasers. A good match between the measured and simulated FMCW LiDAR receive beat signal is achieved with the realistic model parameters used in Table I.

There is, however, some discrepancy between the measured and modeled system noise levels. The different noise components as well as the total noise level for the Gen-1 and Gen-2

chip-scale LiDAR sensors demonstrated here were calculated using Eq. (12) for which some of the parameters are listed in the Table I. The parameters for the ADC quantization noise using a digital oscilloscope were: $V_{ADC} = 1$ V, $N = 8$, and $f_{ADC} = 250$ MHz. For the Gen-1 chip-scale LiDAR, the contributions of the simulated squared noise current from LO shot noise, thermal noise, TIA noise and ADC quantization noise are 1.6×10^{-17} A^2, 2.8×10^{-19} A^2, 2.7×10^{-18} A^2, and 8.5×10^{-18} A^2, respectively, with a total noise current of $\sim 2.8 \times 10^{-17}$ A^2, according to Eq. (12). This translates into an electrical noise floor power level of $\sim 2.8 \times 10^{-11}$ W, or -75.6 dBm using a TIA transimpedance gain of 10^4 V/A used in this LiDAR photoreceiver. It is noted that the calculated shot noise and ADC quantization noise currents of the Gen-1 chip-scale FMCW are about the same order of magnitude. The measured noise floor with the same LiDAR system parameters is about -65 dBm, a discrepancy of ~ 10 dB. The relatively high quantization noise is due to the low ENOB values of 8 for the ADC used in the LiDAR measurements reported here.

For the Gen-2 chip-scale LiDAR, the contributions of the simulated squared noise current from LO shot noise, thermal noise, TIA noise and quantization noise are 8.0×10^{-17} A^2, 6.2×10^{-19} A^2, 2.7×10^{-18} A^2 and 4.2×10^{-17} A^2, respectively. Again, the total noise current value of 1.3×10^{-16} A^2 is not dominated by the LO shot noise but has an ADC quantization noise within a factor of 2 of the shot noise. The simulated noise floor electrical power level is $\sim 2.6 \times 10^{-11}$ W, or -75.9 dBm, similar to the Gen-1 chip-scale LiDAR. The higher LO power level of the Gen-2 LiDAR chip of 1.5 mW is compensated by the lower TIA transimpedance gain of its photoreceiver (4500 V/A) to result in a similar overall noise power. The measured noise floor of the Gen-2 chip-scale LiDAR is also -65 dBm, again resulting in a difference of ~ 10 dB between the modeled and measured noise floor levels. The FMCW LiDAR noise model shown in Eq. (12) does not currently provide an accurate representation of the measured noise floor. One possible explanation could be the FFT bin-to-bin fluctuations in the shot noise. This is not included in the current noise model, which gives an average, not peak noise. Another potential contributor to the FMCW LiDAR noise floor is the laser frequency noise spectrum, which depends on both the laser design and the laser driver electronics noise. More LiDAR noise floor measurements with different photoreceiver electronics configurations and lasers with lower frequency noise can help us understand the source(s) of this discrepancy.

An optimized FMCW LiDAR system design requires that the noise floor be LO shot noise limited for maximum SNR. To this end, the LO optical power level should be increased up to the maximum linear response of the photodetector. In addition, the ADC effective number of bits (ENOB) should be increased to minimize the contribution of the quantization noise to the system noise floor. Both these optimization factors were not implemented in the chip-scale LiDAR prototypes presented here.

The main issue with the Gen-2 chip-scale LiDAR prototype was the rather large effective linewidth (840 kHz) of its integrated laser source, which resulted in a demonstrated maximum

TABLE II
SUMMARY OF PROJECTIONS FOR MAXIMUM ACHIEVABLE RANGE OF NEXT GENERATION CHIP-SCALE LIDAR AS A FUNCTION OF LASER LINEWIDTH AND TRANSMIT OPTICAL POWER, ASSUMING A 10% LAMBERTIAN TARGET. ALSO SHOWN ARE THE PARAMETERS FOR THE GEN-2 CHIP-SCALE LIDAR WITH A DEMONSTRATED RANGE OF 75 M FOR COMPARISON

Chip-Scale LiDAR	Laser Linewidth $\Delta\nu$ [kHz]	Tx Optical Power P_{Tx} [mW]	LO Optical Power P_{LO} [mW]	Target Reflect. ρ_T	Signal / Noise Power P_S / P_S [dBm]	Max Range @10dB SNR R_{max} [m]
Gen-2	840	80	1.5	0.99	-52 /-65	75 (meas.)
Next Gen	100	100	5	0.10	-55/-65	150 (sim.)
Next Gen	100	200	5	0.10	-55/-65	200 (sim.)
Next Gen	10	100	5	0.10	-55/-65	200 (sim.)

range of 75 m with a 99% Lambertian target, as shown in Fig. 12. In order to achieve a LiDAR range of 200 m with a 10% Lambertian target required for most automotive LiDAR applications, both the laser linewidth and transmit optical power need to be improved, assuming other system parameters remain unchanged. Table II summarizes the projected performance of the next generation chip-scale LiDAR optical engine, using the Gen-2 architecture, for different laser linewidths and transmit optical power levels. Also shown in the Table are the parameters for the Gen-2 LiDAR with 75 m demonstrated range for comparison.

We obtained these projections using the model for the FMCW beat signal (Eqs. 10 and 11) with an assumed receive aperture of 9 mm and a system noise floor of -65 dBm. These projections indicate that the chip-scale LiDAR can reach 200 m range at 10 dB SNR with a laser linewidth of 10 kHz and transmit optical power of 100 mW. The same maximum range of 200 m can also be reached with a laser linewidth of 100 kHz by increasing the transmit optical power to 200 mW. Improving the LiDAR system noise floor will further improve the maximum achievable range assuming other parameters remain unchanged.

VII. SUMMARY AND CONCLUSION

In this paper, we first described some of the fundamentals of FMCW LiDAR including a model for the signal-to-noise ratio. This was followed by the demonstration of two novel chip-scale FMCW LiDAR architectures in which the laser sources were fully integrated on the LiDAR Si photonic chips. To the best of our knowledge, this is the first published demonstration of chip-scale FMCW LiDAR with the laser source fully integrated on the LiDAR chip. The realization of these chip-scale LiDAR architectures was enabled by our laser die to Si photonic chip heterogeneous integration technique, which resulted in laser-to-Si waveguide coupling efficiencies as high as 88%. In the first architecture (Gen-1), the LiDAR transmit and receive lights were coupled out of and into the chip via grating couplers, and the LO light was split-off the Si waveguide coupled to the integrated DBR laser source. In the second architecture (Gen2), the LO light was obtained from the back facet of the integrated SGDBR MOPA laser source, the light from the front facet of the laser was directly free-space coupled as the LiDAR transmit beam, and the receive light was coupled to the chip via an edge coupler. We demonstrated maximum ranges of 28 m and 75 m using the Gen-1 and Gen-2 chip-scale LiDAR architectures with

transmit optical power levels of 2 mW and 80 mW, respectively. The measured receive beat signal vs. range for both chip-scale FMCW LiDAR optical engines matched well with the model using justifiable parameters. The measured maximum range for the Gen-1 chip-scale LiDAR was mainly limited by its low transmit optical power of only 2 mW, while that of the Gen-2 chip was limited by the linewidth of the SGDBR laser source. Using the model, we project that the maximum range of the Gen-2 chip-scale LiDAR architecture can be extended to 150-200 m by improving the effective linewidth of the integrated laser source to 10-100 kHz and increasing the LO optical power to 5 mW, while keeping the transmit optical power close to ∼100 mW. Finally, both chip-scale LiDAR optical engines can be coupled to off-chip beam steering elements, such as 2D MEMS scanners, to result in very compact scanning FMCW LiDAR 3D optical sensors.

ACKNOWLEDGMENT

REFERENCES

[1] M. J. Starek, "Airborne laser terrain mapping," in *Encyclopedia of Estuaries*, Berlin, Germany: Springer, Jan.-Dec., 2016. [Online]. Available: https://link.springer.com/referenceworkentry/10.1007%2F978-94-017-8801-4_245

[2] F. Amzajerdian, L. Petway, G. Hines, B. Barnes, D. Pierrottet, and G. Lockard, "Doppler lidar sensor for precision landing on the moon and mars," in *Proc. IEEE Aerosp. Conf.*, 2012, pp. 1–7.

[3] T. Cherian, Y. B. Kumar, and B. S. Reddy, "LIDAR for atmospheric measurements and probing," *Int. J. Eng. Technol.*, vol. 5, no. 6, pp. 5114–5124, Jan. 2013.

[4] U. Weiss and P. Biber, "Plant detection and mapping for agricultural robots using a 3D LIDAR sensor," *Robot. Auton. Syst.*, vol. 59, no. 5, pp. 265–273, May 2011.

[5] J. H. Chumside, "Review of profiling oceanographic lidar," *Opt. Eng.*, vol. 53, no. 5, pp. 051405/1–051405/13, May 2014.

[6] A. P. Dalla Corte *et al.*, "Measuring individual tree diameter and height using gatoreye high-density UAV-Lidar in an integrated crop-livestock-forest system," *Remote Sens*, vol. 12, 2020, Art. no. 863, doi: 10.3390/rs12050863.

[7] R. Turner, R. Panciera, M. A. Tanase, K. Lowell, J. M. Hacker, and J. P. Walker, "Estimation of soil surface roughness of agricultural soils using airborne LiDAR," *Remote Sens. Environ.*, vol. 140, pp. 107–117, Jan. 2014.

[8] M. W. Wachter, A. Rettenmeier, M. Kuhn, and J. Peinke, "Wind velocity measurements using a pulsed LIDAR system: First results," in *Proc. Int. Symp. Adv. Boundary Layer Remote Sens.*, vol. 1, 2008, Art. no. 012066, doi: 10.1088/1755-1307/1/1/012066.

[9] M. Starr, "LIDAR shown to be a powerful new tool in the hunt for missing murder victims," *Sci. Alert*, 2018. [Online]. Available: https://www.sciencealert.com/lidar-unmarked-graves-murder-victims-forensic-science

[10] A. P. Zhevlakov and V. G. Bespalov, "Oil and gas deposits determination by ultraspectral lidar," in *Proc. SPIE*, 2013, Art. no. 9486, doi: 10.1117/12.2177837.

[11] Y. Lou and J. Ibanez-Guzman, "Lidar for autonomous driving: The principles, challenges, and trends for automotive lidar and perception system," *IEEE Signal Process. Mag.*, vol. 37, no. 4, pp. 50–61, Jun. 2020.

[12] J. Hecht, "Lidar for self-driving cars," in *Optics and Photonics*, Washington, DC, USA: OPTICA, 2018.

[13] S. Rangwala, "Do autonomous vehicles need lidar," Forbes Magazine, 2020. [Online]. Available: https://www.forbes.com/sites/sabbirrangwala/2020/04/30/do-autonomous-vehicles-need-lidar/?sh=456dc2b8613f

[14] C. Domke and Q. Potts, "LiDARs for self-driving vehicles," *Autom. World*, 2020. [Online]. Available: https://www.automotiveworld.com/articles/lidars-for-self-driving-vehicles-a-technological-arms-race/io

[15] M. Choudhary, "Why LiDAR is important for autonomous vehicles," *Geospatial World*, 2020. [Online]. Available: https://www.geospatialworld.net/blogs/why-lidar-is-important-for-autonomous-vehicle/

[16] "Silicon photonics: Past, present and future," *Microw. J.*, 2019. [Online]. Available: https://www.microwavejournal.com/articles/32846-silicon-photonics-past-present-and-future

[17] P. Munoz *et al.*, "Silicon nitride photonic integration platform for visible, near-infrared and mid-infrared applications," *Sensors*, vol. 17, no. 9, 2017, Art. no. 2088, doi: 10.3390/s17092088.

[18] L. M. Augustin *et al.*, "InP-based generic foundry platform for photonic integrated circuits," *IEEE J. Sel. Topics Quantum Electron.*, vol. 24, no. 1, Jan./Feb. 2018, Art no. 6100210, doi: 10.1109/JSTQE.2017.2720967.

[19] M. Koskinen, J. Kostamovaara, and R. Myllylae, "Comparison of continuous-wave and pulsed time-of-flight laser range-finding techniques," in *Proc. SPIE*, 1992, Art. no. 1614, doi: 10.1117/12.57989.

[20] P. Feneyrou *et al.*, "Frequency-modulated multifunction lidar for anemometry, range finding, and velocity-1: Theory and signal processing," *Appl. Opt.*, vol. 56, no. 35, pp. 9663–9675, Dec. 2017.

[21] J. Hecht, "Lasers for lidar: FMCW lidar: An alternative for self—driving cars," *LaserFocusWorld*, 2020. [Online]. Available: https://www.laserfocusworld.com/home/article/16556322/lasers-for-lidar-fmcw-lidar-an-alternative-for-selfdriving-cars

[22] A. Martin *et al.*, "Photonic integrated circuit-based FMCW coherent LiDAR," *J. Lightw. Technol.*, vol. 36, no. 19, pp. 4640–4645, Oct. 2018.

[23] Y. Furukado, H. Abe, Y. Hinakura, and T. Baba, "Experimental simulation of ranging action using Si photonic crystal modulator and optical antenna," *Opt. Exp.*, vol. 26, no. 14, pp. 18222–18229, Jul. 2018.

[24] B. J. Isaac, B. Song, S. Pinna, L. A. Coldren, and J. Klamkin, "Indium phosphide photonic integrated circuit transceiver for FMCW LiDAR," *IEEE J. Sel. Topics Quantum Electron.*, vol. 25, no. 6, Nov./Dec. 2019, Art no. 8000107, doi: 10.1109/JSTQE.2019.2911420.

[25] C. V. Poulton *et al.*, "Long-Range LiDAR and free-space data communication with high-performance optical phased array," *IEEE J. Sel. Topics Quantum Electron.*, vol. 25, no. 5, Sep./Oct. 2019, Art. no. 7700108, doi: 10.1109/JSTQE.2019.2908555.

[26] S. A. Miller *et al.*, "512-Element Actively steered silicon phased array for low power LiDAR," in *Proc. Conf. Lasers Electro-Opt.*, 2018, pp. 1–2.

[27] T. Kim *et al.*, "A single-chip optical phased array in a wafer-scale silicon photonics/CMOS 3D-Integration platform," *IEEE J. Solid-State Circuits*, vol. 54, no. 11, pp. 3061–3074, Nov. 2019.

[28] P. Sandborn, "FMCW lidar: Scaling to the chip-level and improving phase-noise-limited performance," Ph.D. dissertation, Dept. Elect. Eng. Comput. Sci., Univ. California at Berkeley, Berkeley, CA, USA, 2019.

[29] T. Kim, "Realization of integrated coherent LiDAR," Ph.D. dissertation, Dept. Elect. Eng. Comput. Sci., Univ. California at Berkeley, Berkeley, CA, USA, 2020.

[30] F. Di Teodoro, "Laser radar and remote sensing: An application-oriented introduction," in *Proc. Conf. Lasers Electro-Opt.*, 2019, pp. 1–3.

[31] imec Si Photonic ICs for Prototyping, [Online]. Available: https://www.imec-int.com/en/silicon-photonic-ICs-prototyping

[32] A. Vasilyev, *The Optoelectronic Swept-Frequency Laser and its Applications in Ranging, Three-Dimensional Imaging, and Coherent Beam Combining of Chirp-Seed Amplifiers*, Pasadena, CA, USA: Dept. Electrical Engineering, California Institute of Technology, 2013.

[33] N. Satyan, A. Vasilyev, G. Rakuljic, V. Leyva, and A. Yariv, "Precise control of broadband frequency chirps using optoelectronic feedback," *Opt. Exp.*, vol. 17, no. 18, pp. 15991–15999, 2009.